Design of A Two-Stage Control Strategy of Vanadium Redox Flow Battery Energy Storage Systems for Grid Application

Citation for the original published paper (version of record):
Xiong, B., Tang, J., Li, Y. et al (2022). Design of A Two-Stage Control Strategy of Vanadium Redox Flow Battery Energy Storage Systems
for Grid Application. IEEE Transactions on Sustainable Energy, 13(4): 2079-2091.
http://dx.doi.org/10.1109/TSTE.2022.3181751

Design of A Two-Stage Control Strategy of Vanadium Redox Flow Battery Energy Storage Systems for Grid Application

Binyu Xiong, *Member, IEEE,* Jinrui Tang, *Member, IEEE,* Yang Li, *Member, IEEE,* Changjun Xie, *Member, IEEE,* Zirui Wang, Xinan Zhang, *Member, IEEE,* and Hoay Beng Gooi, *Life Senior Member*

***Abstract* — The low energy conversion efficiency of the vanadium redox flow battery (VRB) system poses a challenge to its practical applications in grid systems. The low efficiency is mainly due to the considerable overpotentials and parasitic losses in the VRB cells when supplying highly dynamic charging and discharging power for grid regulation. Apart from material and structural advancements, improvements in operating strategies are equally essential for achieving the expected high-performance VRB system, although an optimized solution has not been fully exploited in the existing studies. In this paper, a two-stage control strategy is thus developed based on a proposed and experimental validated multi-physics multi-time-scale electro-thermo-hydraulic VRB model. Specifically, in the first stage, the optimal flow rate of the VRB is obtained based on online optimization to reduce parasitic loss and enhance instantaneous system efficiency, and the result serves as the set point of a feedback flow rate controller. In the second stage, dual time scales are specifically considered. And the current and flow rate controllers are designed to meet the highly varying power demands for grid-connected applications. The effectiveness of the proposed control strategy is verified under a scenario to smooth wind power generation. Comparative studies show that compared to the prevailing approaches, higher efficiency can be achieved in tracking the theoretical optimal power profiles for online battery control.**

Index Terms—vanadium redox flow battery, multi-physics model, optimal operation, control strategy, system efficiency.

NOMENCLATURE

A_p	Cross-sectional area of the pipe
A_{ec}	Graphite plate channels cross-section overall area
A_{ed}	Electrode surface area
C_{th}	Heat capacity
C_{norm}	Rated capacity of the VRB
D_p	Hydraulic diameter of the pipe
E_0	Standard formal potential
$E_0^{T_0}$	The standard formal potential at room temperature
F	Faraday constant
I	Applied current
N	The number of cells in a stack
Q	Electrolyte flow rate
R	Gas constant
z	Electrons transferred in the redox reaction
I_{ref}	Optimal reference of current
K_1, K_2	Line flow tee coefficient, brand flow tee
K_{ck}	Carman-Kozeny constant
K_{form}	Form coefficient of pipe
L_p	Length of pipe
P_Σ	Total power loss
$P_{Ch/Dis}$	Net power from/to the grid
P_{entro}	Heat generated
Q_{ref}	Optimal reference of flow rate
Q_{ctrl}	Actual control flow rate
R_b	Resistance of the bipolar plate
R_e	Resistance of the electrolyte
R_m	Resistance of the membrane
R_{th}	Thermal resistance
R_{ohm}	Ohmic resistance
$R_{ohm}^{T_0}$	Ohmic resistance at room temperature
$R_{self\text{-}shunt}$	Shunt and self-discharge resistance
$T_{Q\text{-}adj}$	Flow rate adjusted at a period of time
U_{av}	Average voltage
$V_{branch,k}$	Velocity of the electrolyte in the kth branch
c_v	Total vanadium concentration
c_{bulk}	Bulk concentration of active species
i_0	Exchange current density on electrode surface
k_1, k_2	Correction coefficients
$k_{i,I}$, $k_{i,Q}$	Integral coefficients
$k_{p,I}$, $k_{p,Q}$	Proportional coefficients
$t_{self\text{-}shunt}$	Duration of the experiment
σ	Conductivity of the electrolyte
ρ	Density of the electrolyte
μ	Viscosity of the electrolyte
ε	Porosity of the graphite felt electrode
f_p	Friction coefficient of pipe
d_f	Fiber diameter of the electrode
η_{ohm}	Ohmic overpotential
η_{act}	Activation overpotential
η_{con}	Concentration overpotential
τ_{pump}	Pump efficiency
$\Delta p_{friction}$	Pressure drop due to friction loss
Δp_{form}	Pressure drop due to form loss
Δp_{total}	Total pressure drop in the VRB

This work is supported by National Science Foundation of China (#52177221, # 51977164). *(Corresponding author: Jinrui Tang)*

Binyu Xiong, Jinrui Tang, and Changjun Xie are with the School of Automation, Wuhan University of Technology, Wuhan 430070, China (e-mail: bxiong2@whut.edu.cn; tangjinrui@whut.edu.cn; jackxie@whut.edu.cn).

Yang Li is with the School of Automation, Wuhan University of Technology, Wuhan 430070, China, and also with the Department of Electrical Engineering, Chalmers University of Technology, 41296 Gothenburg, Sweden (e-mail: yangli@ieee.org).

Zirui Wang is with Jiangmen Southern Power Grid Company (e-mail: 516423435@qq.com).

Xinan Zhang is with University of Western Australia, Perth, Australia (e-mail: xinan.zhang@uwa.edu.au).

Hoay Beng Gooi is with Nanyang Technological University, Singapore, Singapore (e-mail: ehbgooi@ntu.edu.sg).

I. Introduction

LARGE-SCALE energy storage systems (ESSs) play critical roles in coping with the challenges of harnessing energy from fluctuating and intermittent renewable sources such as wind and solar [1-3]. Thanks to the advantages of ensured safety, long service lifetime, ease of recycling, and flexible design with independent power and capacity ratings, worldwide deployment of the vanadium redox flow battery (VRB) ESSs has increased rapidly in modern power grid systems. However, compared to the prevailing electrochemical storage devices, such as lithium-ion (Li-ion) batteries, VRB-ESSs have much lower energy conversion efficiencies due to their high overpotentials and parasitic losses. For example, the overall round-trip efficiency of a Li-ion battery is usually around 90−98%, whereas the efficiency of a typical VRB-ESS is only up to 80−85% [4,5]. Hence, a large amount of energy will be wasted during the frequent charging and discharging processes. This fact hinders the popularization and commercialization of VRB-ESSs [6-8].

The unsatisfactory performance of VRB systems motivates active research devoted to increasing energy conversion efficiency, and fruitful outcomes have been gained in the past. For example, to reduce the ohmic and concentration overpotentials, some studies are focused on the improvement and optimized design of key components such as the electrode [9], membrane [10], and stack [11]. The second path is to develop improved internal state monitoring and novel control strategies, to reduce the parasitic losses during operation [12-13]. For instance, the electrolyte flow rate is one of the unique features of the VRB that affects the speed of delivering active species to the stack. A higher electrolyte flow rate can reduce concentration overpotential and enhance voltage efficiency [14]. However, it will also increase pump power consumption, resulting in higher parasitic loss and reduced system efficiency [15]. This trade-off between the concentration overpotential and the parasitic loss has been considered for designing optimal operational strategies.

Early research focused on obtaining the optimal flow rate via offline experiments, and the designed strategies can only be implemented as open-loop control. For example, Ling *et al.* [16] adopted a pulsing electrolyte flow strategy to reduce the parasitic loss by switching on/off the pumps. Ma *et al.* [17] found out that a step-up of the flow rate at the end of the charge or discharge process can reduce high concentration overpotential. With such a strategy, the system efficiency can be improved by 8% compared with a constant flow rate strategy. To further improve the performance via manipulating the flow rate, the *flow factor* (FF) was defined by Tang *et al.* in [18]. It was demonstrated that a flow rate with FF = 7.5 could achieve the highest system efficiency under the constant current charge/discharge condition. König *et al.* [19] extended this concept and developed a variable flow factor strategy for a specific operating point defined by the state of charge (SOC) and the applied current. Xiao *et al.* [20] later modified the flow factor as a power function of SOC. The variation of pump efficiency with flow rate was considered in their work. Indeed, these open-loop control methods are easy to implement. Unfortunately, since the flow rate references were prerequisites from offline experiments, these methods usually lack robustness to model parameter changes and disturbances.

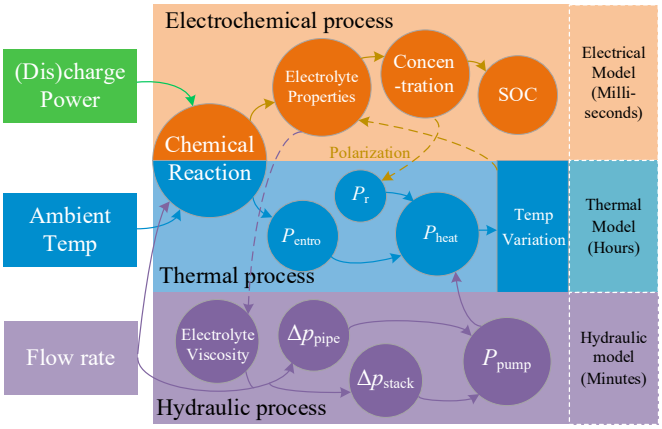

Fig. 1. Coupling relationship of multi-physics of the VRB.

Various closed-loop control systems were further proposed to tackle the problems of the open-loop methods. For example, Li *et al.* [21] used a classic proportional-integral (PI) controller to adjust the electrolyte flow rate and track the desired reference trajectory with high precision. Pugach *et al.* [22] designed a robust feedback device to track the optimal reference voltage, effectively reducing the pump loss. Rajagopalan *et al.* [23] proposed a VRB charging strategy based on fuzzy control to reduce the parasitic loss of the system and ensure the VRB has good dynamic characteristics. It should be noted that these control strategies are developed under constant current/power charging/discharge mode from extensive laboratory tests. However, the constant current/power assumption becomes invalid for practical applications such as renewable power smoothing or peak shaving. In practice, the operating conditions are very dynamic, and the assigned power to the VRB system is always highly fluctuating. To further consider more practical and complex operating conditions, Wang *et al.* [24] recently proposed a dynamic flow control strategy to smooth the generated power. With the strategy, the system efficiency can reach 87.7% on a typical summer day, and the electrolyte temperature can be maintained within a safe range despite the high ambient temperature. Furthermore, Jirabovornwisut *et al.* [25] proposed a heuristic control strategy to ensure high round-trip efficiency by minimizing the charging energy and maximizing the discharge energy.

Although the previous works have contributed significantly to the advancements of VRB system control, further improvements in system efficiency become challenging. The major limitation is due to that the controllers in the existing schemes were designed independently by ignoring the coupling effects between the multiple physical processes in the VRBs. This simplification can make the controllers easy to design and simple to implement with several pre-set optimal operating points [18, 22-24]. However, as schematized in Fig. 1, in a VRB, there are coupled multi-physics relationships involving electrochemical, thermal, and hydraulic processes [20, 26-29]. Once the pre-designed operation conditions vary, the system dynamics cannot be adaptively adjusted to a new optimal operating point, leading to decreased system efficiency.

In addition, the time scales of these physical processes differ significantly, whereas this fact has not been adequately considered in the existing control strategies, leading to low effectiveness. Specifically, the electrochemical process is the fastest process, occurring in milliseconds. The hydraulic transport process has a larger time constant in the order of several minutes due to the hydraulic inertia of the system and the transfer of ions in the pipes [22, 30]. Furthermore, since the electrolyte temperature would rise after cycles due to the entropic, joule, and parasitic heat dissipations, the thermal dynamic process has the longest time scale. The time constant can be several hours, depending on the scalability of the system and heat convection coefficient [31]. It should be noted that frequent adjustment of the flow rate would significantly reduce the reliability and longevity of the pumps. Therefore, it will be beneficial to coordinate different time scales for controller design.

In this paper, to improve the efficiency of the VRB system under practical grid operating conditions, a two-stage optimal control strategy based on a multi-physics multi-time-scale model is developed. In the proposed strategy, the first stage obtains the global optimal operating points under various grid conditions by taking the coupled effects of the VRB into account. The second stage considers the time-scale differences between the current control and the flow rate control loops, leading to a simple design with excellent tracking performance, while temperature control is assumed to be designed independently due to its much longer time scale. The main contributions of this paper can be summarized as follows: 1) A two-stage control strategy is designed to achieve maximal system efficiency. The proposed strategy could optimize both the flow rate and current as a whole. The reference value of the flow rate and current are obtained in the first stage; 2) A multi-physics model reflecting the coupling effects of three physical processes is proposed in the first stage, and a dual time-scale controller consisting of a flow rate controller for the pumped electrolyte transfer in a slow time scale and a fast time scale current controller is designed in the second stage. To present the novel control scheme, the rest of our paper is organized as follows. In Section II, a multi-physics model is established firstly to reveal the coupling effects of three physical processes and verified experimentally using a 5-kW/3-kWh VRB system. The proposed two-stage control scheme is presented in Section III. Simulation results under the grid application scenarios for mitigating wind power fluctuation are given in Section IV. Finally, the conclusions are drawn in Section V.

II. Model Development

A multi-physics model of VRBs incorporating three physical processes is first established in this section to reveal the coupling effects of the flow rate, current, and temperature. As shown in Fig. 2, the multi-physics model includes an electrical circuit submodel, a hydraulic submodel, and a thermal submodel.

A. Electrical Submodel

The electrical submodel emulates the electrochemical process

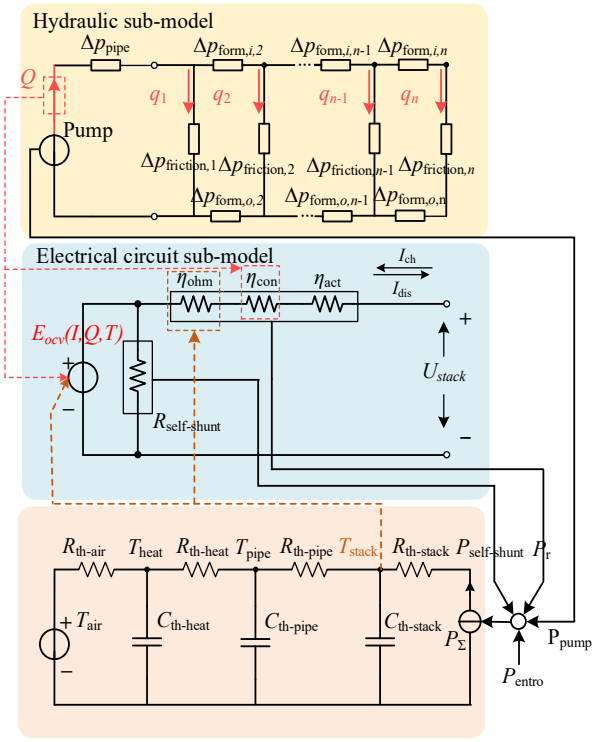

Fig. 2. Multi-physics equivalent circuit model of the VRB.

of VRBs. As shown in Fig. 2, the open-circuit voltage (OCV) source, E_{ocv}, derived from the Nernst equation, represents the thermodynamic equilibrium potential of VRB stacks, i.e.,

$$E_{\text{ocv}} = E_0 + N\frac{RT_{\text{stack}}}{zF}\ln\left(\frac{c_{\text{VO}_2^+}c_{\text{V}^{2+}}c_{\text{H}^+}^2}{c_{\text{V}^{3+}}c_{\text{VO}^{2+}}}\right) \tag{1}$$

$$E_0 = E_0^{T_0} - k_T(T_{\text{stack}} - T_0) \tag{2}$$

where E_0 is the standard formal potential and T_{stack} is the stack temperature. $c_{\text{VO}_2^+}$, $c_{\text{V}^{2+}}$, $c_{\text{V}^{3+}}$, $c_{\text{VO}^{2+}}$, and c_{H^+} denote the outlet concentrations of various valence vanadium ions and hydrogen ion, respectively. N is the number of cells in a stack, R is the gas constant, z is electrons transferred in the redox reaction, F is the Faraday constant, $E_0^{T_0}$ is the standard formal potential at the reference temperature T_0 = 298.15 K, and k_T denotes a temperature correction coefficient. The SOC of the VRB is defined as

$$\text{SOC} = \frac{c_{\text{V}^{2+}}}{c_{\text{V}^{2+}} + c_{\text{V}^{3+}}} = \frac{c_{\text{VO}_2^+}}{c_{\text{VO}_2^+} + c_{\text{VO}^{2+}}} \tag{3}$$

The vanadium concentration of a cell is given as

$$c_{\text{V}^{2+}} = c_{\text{VO}^{2+}} = \text{SOC}\cdot c_v + \frac{I}{zFQ} \tag{4}$$

where I is the applied current, defined as positive during the charging process, Q denotes the electrolyte flow rate, and c_v denotes the total vanadium concentration in the solution.

Considering c_{H^+} = 1 and using (3) and (4), one can eliminate the concentration terms in (1) to obtain an expression of the E_{ocv} as a function of I, Q, and T_{stack}. In practice, two coefficients k_1 and k_2 are used to correct the relationship between SOC and the OCV, given by,

$$E_{\text{ocv}}(I,Q,T_{\text{stack}}) = E_0 + N\frac{2RT_{\text{stack}}}{zF}\left\{k_1 \ln\left(\text{SOC}+\frac{I}{zFQ}\right)+ k_2 \ln\left[1-\left(\text{SOC}+\frac{I}{zFQ}\right)\right]\right\} \quad (5)$$

The ohmic overpotential η_{ohm} in Fig. 2 represents the voltage drop from the bipolar plate, membrane, and electrolyte. It is expressed as

$$\eta_{\text{ohm}} = I(R_b + R_m + R_e) = IR_{\text{ohm}} \quad (6)$$

where R_b, R_m, and R_e denote the equivalent resistances of the bipolar plate, membrane, and electrolyte, respectively. R_{ohm} is the sum of the three resistances. Temperature is a significant factor affecting the ohmic overpotential in (7), i.e.,

$$R_{\text{ohm}} = R_{\text{ohm}}^{T_0} - k_R(T_{\text{stack}} - T_0) \quad (7)$$

where $R_{\text{ohm}}^{T_0}$ denotes the ohmic equivalent resistance R_{ohm} at T_0 and k_R is a temperature correction coefficient.

The activation overpotential η_{act} in Fig. 2 describes the charge-transfer controlled kinetics of an electrochemical reaction, expressed by

$$\eta_{\text{act}} = N\frac{2RT_{\text{stack}}}{zF}\ln\left(\frac{i_0}{I/A_{\text{ed}}}\right) \quad (8)$$

where i_0 is the exchange current density on the electrode surface and A_{ed} is the electrode surface area. The activation overpotential is predominant under small currents, but it can be significantly reduced due to the large effective surface areas in a VRB with porous electrodes.

The concentration overpotential, η_{con}, results from the mass transfer limitation caused by the concentration gradient between the volume electrolyte solution and the electrode surface. η_{con} is described with the addition of the concentration correction coefficient as [18]

$$\eta_{\text{con}} = -k_3 \cdot \frac{RT_{\text{stack}}}{zF}\ln\left(1-\frac{I}{1.6\times10^{-4}\times zFA_{\text{ed}}(Q/A_{\text{ec}})^{0.4}c_{\text{bulk}}}\right) \quad (9)$$

where c_{bulk} denotes the bulk concentration of the active species, which is presented in Table I. A_{ec} denotes the graphite plate channel overall cross-sectional area.

Thus, the stack voltage can be expressed by incorporating the overall overpotential as

$$U_{\text{stack}} = E_{\text{ocv}} + \eta_{\text{ohm}} + \eta_{\text{act}} + \eta_{\text{con}} \quad (10)$$

Furthermore, the shunt/self-discharge resistance, $R_{\text{self-shunt}}$, is determined by electrolyte conductivity and specific fluid-frame design. In this paper, $R_{\text{self-shunt}}$ is estimated by an experimental method, calculated by

$$R_{\text{self-shunt}} = \frac{U_{\text{av}}t_{\text{self-shunt}}}{C_{\text{norm}}} \quad (11)$$

where U_{av} denotes the average voltage in the experiment, $t_{\text{self-shunt}}$ denotes the duration of the experiment, and C_{norm} denotes the rated capacity of the VRB.

B. Hydraulic Submodel

The electrolytes are circulated in the hydraulic pipes and driven by the pumps. In general, the pump power (or parasitic loss), consumed to overcome the fluid friction flowing through the stacks and hydraulic circuits, is mainly determined by the pressure drop and flow rates, i.e., [32]

TABLE I
BULK CONCENTRATION OF THE ACTIVE SPECIES

c_{bulk}	Charge Mode	Discharge Mode
Positive electrode	$c_{VO^{2+}}$	$c_{VO_2^+}$
Negative electrode	$c_{V^{3+}}$	$c_{V^{2+}}$

$$P_{\text{pump}} = (\Delta p_{\text{total}} \times Q)/\tau_{\text{pump}} \quad (12)$$

where τ_{pump} denotes the pump efficiency, Δp_{total} denotes the total pressure drop in the VRB. The total pressure drop can be divided into two parts for the stack and the pipe:

$$\Delta p_{\text{total}} = \Delta p_{\text{stack}} + \Delta p_{\text{pipe}} \quad (13)$$

The pressure drop in the hydraulic circuits occurs when the electrolytes run through the pipes. The hydraulic pressure drop is given as below,

$$\Delta p_{\text{pipe}} = \frac{\rho}{2A_p^2}\left(f_p\frac{L_p}{D_p} + K_{\text{form}}\right)Q^2 \quad (14)$$

where ρ denotes the density of the electrolyte, A_p, f_p, L_p, D_p, and K_{form} represent the cross-sectional area, friction coefficient, length, hydraulic diameter, and form coefficient of the pipe, respectively.

The pressure drop in the stack can be obtained by the form loss and the friction loss:

$$\Delta p_{\text{stack}} = \sum_{k=1}^{N}\Delta p_{\text{friction},k} + \sum_{k=2}^{N}(\Delta p_{\text{form},i,k} + \Delta p_{\text{form},o,k}) \quad (15)$$

The pressure drop in the kth cell of the stack can be expressed as,

$$\Delta p_{\text{form},i,k} + \Delta p_{\text{form},o,k} = K_1 V_{\text{branch},k}^2/2 + K_2 V_{\text{branch},k}^2/2 \quad (16)$$

where K_1 denotes the line flow tee coefficient, K_2 denotes the branch flow tee, and $V_{\text{branch},k}$ denotes the velocity of the electrolyte in the kth branch.

The pressure drop due to friction loss in the kth cell of the stack can be expressed as

$$\Delta p_{\text{friction},k} = \left(\mu\frac{K_{\text{ck}}(1-\varepsilon)^2}{\varepsilon^3 d_f^2}\right)V_{\text{branch},k}L_k \quad (17)$$

where μ is the viscosity of the electrolyte, ε denotes the porosity of the graphite felt electrode, d_f indicates the mean fiber diameter of the electrode, K_{ck} represents the Carman-Kozeny constant, and L_k is the distance between the inlet pipe and the outlet pipe.

C. Thermal Submodel

Temperature variation affects the electrochemical reaction rate, thermal properties of electrolytes, the resistivity of materials, and therefore the external characteristic of VRBs. The thermal model of VRB is represented by the 3rd-order Causer network [28],

$$C_{\text{th-stack}}\frac{dT_{\text{stack}}}{dt} = -\frac{1}{R_{\text{th-pipe}}}T_{\text{stack}} + \frac{1}{R_{\text{th-pipe}}}T_{\text{pipe}} + P_{\Sigma} \quad (18)$$

$$C_{\text{th-pipe}}\frac{dT_{\text{pipe}}}{dt} = \frac{1}{R_{\text{th-pipe}}}T_{\text{stack}} - \left(\frac{1}{R_{\text{th-heat}}} + \frac{1}{R_{\text{th-pipe}}}\right)T_{\text{pipe}} + \frac{1}{R_{\text{th-heat}}}T_{\text{heat}} \quad (19)$$

$$C_{\text{th-heat}}\frac{dT_{\text{heat}}}{dt}=\frac{1}{R_{\text{th-heat}}}T_{\text{pipe}}-\left(\frac{1}{R_{\text{th-air}}}+\frac{1}{R_{\text{th-heat}}}\right)T_{\text{heat}}+\frac{1}{R_{\text{th-air}}}T_{\text{th-air}} \quad (20)$$

where the symbols R_{th}, C_{th}, and T represent the thermal resistance, heat capacity, and temperature in the corresponding components or environments, respectively. Furthermore, P_{Σ} represents the total power loss, consisting of four terms, i.e.,

$$P_{\Sigma}=P_{\text{entro}}+P_{\text{pump}}+P_{\text{self-shunt}}+P_{r} \quad (21)$$

where P_{entro} denotes the heat generated due to electrochemical reactions, P_{pump} is the pump power calculated by (12), $P_{\text{self-shunt}}=E_{\text{ocv}}^2/R_{\text{self-shunt}}$ denotes the shunt current loss, and P_r denotes the power loss due to the overpotential inside the stack, expressed by

$$P_r=P_{\text{ohm}}+P_{\text{act}}+P_{\text{con}}=I^2R_{\text{ohm}}+I\eta_{\text{act}}+I\eta_{\text{con}} \quad (22)$$

III. Two-Stage Control Strategy

In this section, a two-stage control strategy considering the different time scales system dynamics is proposed to achieve maximum system efficiency. The first stage is the multi-variable coordinated optimization. At this stage, the optimal flow rate and current references are obtained by an optimizer. The second stage is a dual-time-scale control stage that includes a long-term flow rate controller and a short-term current controller. At this stage, the flow rate is discretely adjusted at the end of the charge/discharge process to seek a balance between the overpotential loss and the parasitic loss.

A. Control Objective

The control objective is to achieve maximum system efficiency under dynamic discharge/charge power requirements. Conventionally, the system efficiency of VRB is defined as the ratio of the released energy to the absorbed energy in one full charge/discharge cycle. However, this definition is not applicable for real-time operation since a complete cycle is rarely experienced. A new index, the instantaneous system efficiency (*ISE*), is therefore defined here to describe the real-time performance of the battery, i.e.,

$$ISE=\frac{P_{\text{Ch/Dis}}}{P_{\text{Ch/Dis}}+P_{\Sigma}} \quad (23)$$

where $P_{\text{Ch/Dis}}$ is the net power exchange with the grid.

The maximum *ISE* is obtained by solving an optimization problem, i.e.,

$$\max\left(ISE\right)\Rightarrow\min\left(1-ISE\right)=\min\left(\frac{P_{\Sigma}}{P_{\text{Ch/Dis}}+P_{\Sigma}}\right) \quad (24)$$

TABLE II
OPERATING CONSTRAINTS OF THE VRB SYSTEM

Parameters	Constraints
Power Balance	$P_{\text{Ch/Dis}}=U_{\text{stack}}\times I$
Input/Output Power	$P_{\min}\le P_{\text{Ch/Dis}}\le P_{\max}$
SOC	$\text{SOC}_{\min}\le\text{SOC}\le\text{SOC}_{\max}$
Terminal Voltage	$U_{\min}\le U_{\text{stack}}\le U_{\max}$
Charge/Discharge Current	$I_{\min}\le I\le I_{\max}$
Flow Rates	$Q_{\min}\le Q\le Q_{\max}$
Temperature	$T_{\min}\le T_{\text{stack}}\le T_{\max}$

and the operating limits such as power balance, flow rates, and temperature are considered as the constraints, as given in Table II.

B. Control Framework

The control frame consists of two stages, including 1) a multi-variable coordinated stage, which provides the flow rate and current reference values for the second stage, and 2) a dual-time-scale controller, which combines two different time scales of current and flow rate controllers.

The control framework of the proposed two-stage control strategy is shown in Fig. 3. In the first stage, flow rate reference Q_{ref} is obtained based on the proposed model and demand power. These references are sent to the second stage, where the flow rate reference is modified by considering the hydraulic inertia. As mentioned earlier, the time scales of flow rate and current are in order of minutes and milliseconds, respectively.

The first stage is described below:

Step 1: Given the initial flow rate Q_0, SOC, T_{stack}, and (Dis)charge power $P_{\text{Ch/Dis}}$.

Step 2: Obtain a nonlinear function $F(I_k, Q_k, \text{SOC}, T_{\text{stack}},$

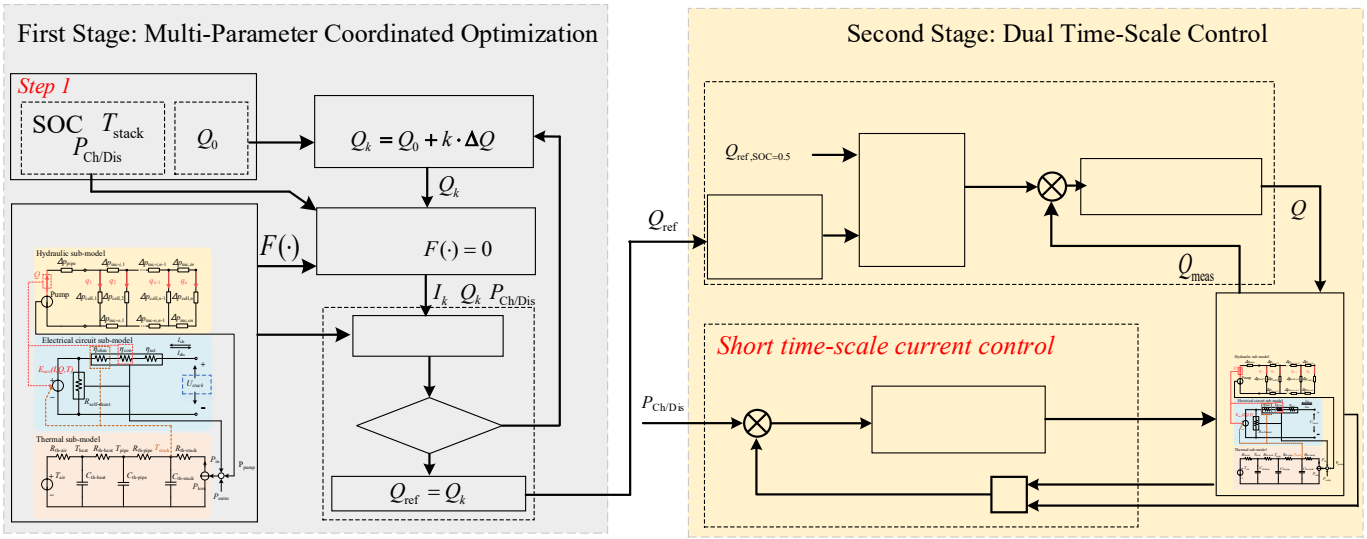

Fig. 3. Framework of the proposed two-stage control strategy of VRB system.

$P_{\text{Ch/Dis}}$), using the multi-physics model.

Step 3: Obtain the flow rate sequence. The flow rate is discrete and represented as $[Q_0, Q_1, \ldots, Q_k, \ldots, Q_n]$, $k = 0, 1, 2, \ldots, n$ by (25), where $Q_0 \in [Q_{\min}, Q_{\max}]$

$$\begin{cases} Q_k = Q_0 + k \cdot \Delta Q \\ \Delta Q = (Q_{\max} - Q_{\min}) / n \end{cases} \tag{25}$$

Step 4: Obtain the candidate current reference under the power balance constraint: For each Q_k, solve the nonlinear equation $F(I_k, Q_k, \text{SOC}, T_{\text{stack}}, P_{\text{Ch/Dis}}) = 0$ for I_k with the gradient descent method.

Step 5: Find the optimal references to achieve the maximum *ISE*.

$$[Q_{\text{ref}}, I_{\text{ref}}] = \arg\max_{Q_k, I_k}(ISE) \tag{26}$$

The second stage is a dual time-scale controller that consists of a flow rate controller and a current controller. The actual reference to control flow rate, denoted by Q_{ctrl}, is affected by battery SOC. If the battery SOC is within the range of 0.3 to 0.7, the flow rate is kept constant as $Q_{\text{ctrl}} = Q_{\text{ref,SOC=0.5}}$. If the battery

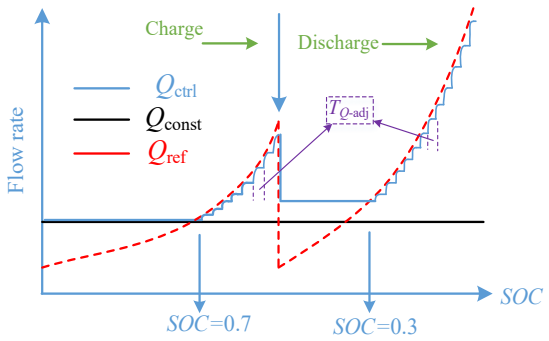

Fig. 4. Proposed flow rate adjustment strategy for second stage.

SOC is below 0.3 or above 0.7, the flow rate will be adjusted to overcome the excessive concentration overpotential. The flow rate is controlled in a discrete manner with a sample time of T_{Q_adj} to avoid overly damaging effects on the pumps. The proposed flow rate strategy is illustrated in Fig. 4.

The flow rate and the current are regulated by two PI controllers, respectively, e.g.,

$$\begin{cases} Q(t) = k_{p,Q} e_Q(t) + k_{i,Q} \int_0^t e_Q(\tau) d\tau \\ e_Q(t) = Q_{\text{ctrl}}(t) - Q_{\text{meas}}(t) \end{cases} \tag{27}$$

$$\begin{cases} I(t) = k_{p,I} e_I(t) + k_{i,I} \int_0^t e_I(\tau) d\tau \\ e_I(t) = P_{\text{Ch/Dis}}(t) - U_{\text{stack}} I_{\text{meas}}(t) \end{cases} \tag{28}$$

where $k_{p,Q}$ and $k_{i,Q}$ are the proportional and integral gains, respectively; $k_{p,I}$ and $k_{i,I}$ are the proportional and integral gains of the current PI controller, respectively; Q_{meas} and I_{meas} are measured flow rate and current, respectively.

TABLE III
SPECIFICATION OF THE EXPERIMENTAL VRB SYSTEM

Configuration	Value
Power rating	5 kW
Capacity	3 kWh
Number of cells	37
Terminal voltage constraints	[40, 60] V
Flow rate constraints	[50,500] $\text{cm}^3 \cdot \text{s}^{-1}$
Temperature constraints	[−5, 35] °C
Stack dimension	75 cm×48 cm×30 cm
Concentration of vanadium ion	1.5 $\text{mol} \cdot \text{L}^{-1}$
Electrolyte volume	200 L

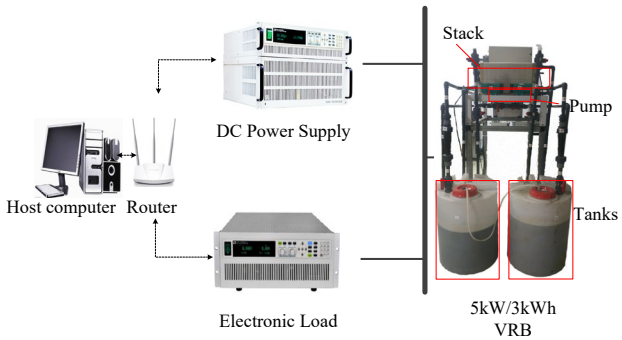

Fig. 5. 5-kW/3-kWh VRB experiment platform.

IV. ILLUSTRATIVE EXAMPLES

A. Multi-Physics Model Validation

A 5-kW/3-kWh VRB experimental platform was set up in our laboratory. As shown in Fig. 5, the platform includes a host computer, a DC power supply, and a DC electronic load power supply. The specification and operation constraints of the VRB are given in Table III.

The experiment was designed and carried out to validate the proposed multi-physics VRB model. Charging/discharging data were collected under constant current and pulse current tests at a flow rate of 300 $\text{cm}^3 \cdot \text{s}^{-1}$. The key parameters used in the multi-physics models are listed in Table IV, which were obtained from experiments and the literature. Specifically, for the electrical submodel, since the expressions of the OCV and the concentration overpotential are nonlinear, the particle swarm optimization (PSO) method is selected to identify the parameters such as, $E_0^{T_0}$, $R_{\text{ohm}}^{T_0}$, k_1, k_2, and k_3. The deduction details are elaborated in Appendix A. For the hydraulic submodel, the key parameters such as K_{form}, μ, and ρ are obtained from [26, 32]. The parameters of the thermal submodel were obtained from our previous study, which is shown in

TABLE IV
KEY PARAMETERS IN THE MULTI-PHYSICS MODEL

Electrical circuit submodel			
Parameter	Value	Parameter	Value
$E_0^{T_0}$	52.3 V	$R_{\text{ohm}}^{T_0}$	0.046 Ω
k_T	4.66×10^{-2}	k_R	5×10^{-4}
k_1	1.3389	A_{cd}	0.72 m^2
k_2	1.3255	A_{ec}	2×10^{-6} m^2
k_3	1.5	$R_{\text{self-shunt}}$	83.33 Ω
Hydraulic submodel			
Parameter	Value	Parameter	Value
τ_{pump}	85%	K_{form}	2.1
ρ	1400 $\text{kg} \cdot \text{m}^{-3}$	μ	7×10^{-3} Pa·s
A_p	3.14×10^{-4} m^2	d_f	3×10^{-15} m
f_p	0.015	ε	0.68
L_p	3.56 m	K_{ck}	5
D_p	0.01 m		
Thermal submodel			
Parameter	Value	Parameter	Value
$C_{\text{th-stack}}$	4760 F	$R_{\text{th- pipe}}$	1×10^{-3} Ω
$C_{\text{th-pipe}}$	5.2×10^4 F	$R_{\text{th-heat}}$	3.8×10^{-3} Ω
$C_{\text{th-heat}}$	4.7×10^5 F	$R_{\text{th-air}}$	8.4×10^{-3} Ω
$R_{\text{th-stack}}$	2.1×10^4 Ω		

Appendix B [28]. Furthermore, a self-discharge experiment was carried out: During the battery self-discharge process with running pumps, the SOC drops from 100% to 5% in 105 h. This result can be used to identify the parameter $R_{\text{self-shunt}}$ according to (10).

The model validation results are shown in Fig. 6, where the sensitivities to various factors are also illustrated. In Fig. 6(a), the simulation results are compared with the experimental data. The proposed multi-physics model is validated under constant charge/discharge currents of 60 A, 80 A, and 100 A. The results show that the root-mean-square error (RMSE) of the voltage profile is 0.62 V. The maximum absolute error is 1.95 V, or 3.9% of the nominal stack voltage of 50 V. The simulation results show that the proposed model fits well with the experimental data, and thus, it is capable of describing multi-physics behavior accurately. The pump power losses under various flow rates are analyzed and shown in Fig. 6(b) for the sensitivity study. It can be seen that, as the flow rate increases, the pump power loss increases drastically. From the stack voltages of the proposed model under various flow rates and temperatures in Fig. 6(c) and Fig. 6(d), we observe that both the flow rate and the temperature can significantly affect the battery voltage. These phenomena are expected and backed by physical principles. For example, the temperature drop causes the increase of the standard formal potential, leading to an increase in stack voltage.

With the proposed model, the predicted temperatures of the stack, pipe, and heat exchanger cycled with constant charging/discharging power are shown in Fig. 7. The average ambient temperature of 11 °C is assumed. It is observed that the stack temperature is always the highest. In the first two cycles, the temperature rises rapidly, after which the temperature tends to be stabilized.

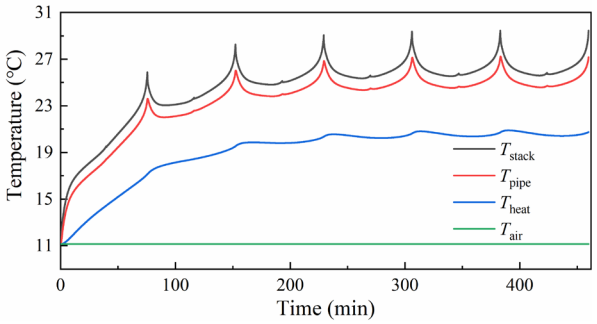

Fig. 7. Temperature prediction of VRB under constant power 4 kW scenario.

B. *Analysis of Two-Stage Control Strategy*

The VRB absorbs or releases a certain amount of power according to the power demand. In this section, an analysis of the proposed two-stage control strategy is carried out by simulation. The optimal flow rate and current are searched according to the steps of Stage 1 to achieve the highest *ISE*. The optimal combination of flow rate and current under constant power of 4 kW is listed in Table V.

TABLE V
OPTIMAL FLOW RATES AND CURRENTS AT DIFFERENT SOCS UNDER CONSTANT POWER OF 4 KW

Battery states	SOC	I_{ref} (A)	Q_{ref} (cm^3·s^{-1})
Charge	0.1	78.88	58
	0.3	75.03	65
	0.5	72.74	75
	0.7	70.53	94
	0.9	66.80	164
Discharge	0.9	74.45	61
	0.7	78.67	75
	0.5	81.66	91
	0.3	85.14	123
	0.1	92.89	262

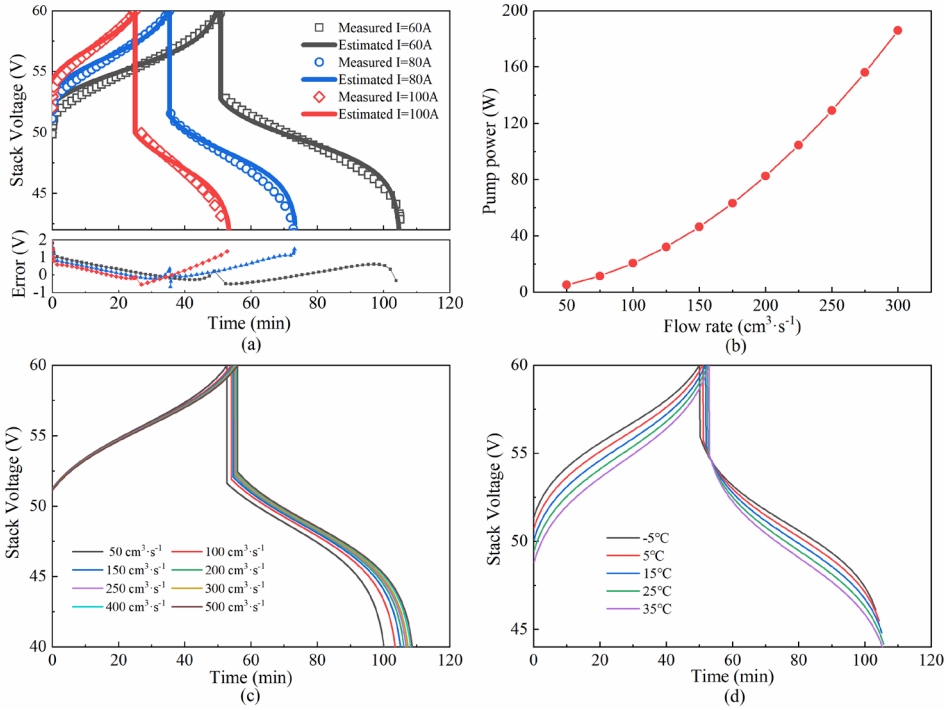

Fig. 6. Model validation and model sensitivity under various operation factors: (a) Stack voltage curves at different currents;(b) Pump power under different flow rates; (c) Stack voltage curves at various flow rates; (d) Stack voltage curves under different temperatures.

Furthermore, the optimal flow rates under various charge/discharge power and SOCs are plotted in Fig. 8. As the demand power increases, the optimal flow rate increases as well. Meanwhile, as the SOC reaches the lower/upper value, the slope of the optimal flow rate increases sharply. For instance, the optimal flow rate is around 80 $cm^3 \cdot s^{-1}$ at SOC = 0.5 when the charge/discharge power is 2 kW. However, the optimal flow rate could reach 350 $cm^3 \cdot s^{-1}$ at SOC = 0.1 under a discharge power of 4 kW. According to (9), the main reason for this phenomenon is the high concentration overpotential due to the depletion of vanadium ions. Another observation is that the optimal flow rate during the discharging process is higher than that during the charging process. For example, the optimal flow rate is 126 $cm^3 \cdot s^{-1}$ at SOC = 0.9 when the charging power is 3kW. But the flow rate is 185 $cm^3 \cdot s^{-1}$ at SOC = 0.1 when the discharging power is 3 kW. This is because the optimal current during the discharging process is often higher than the optimal current during the charging process, according to (11) and the power balance conditions.

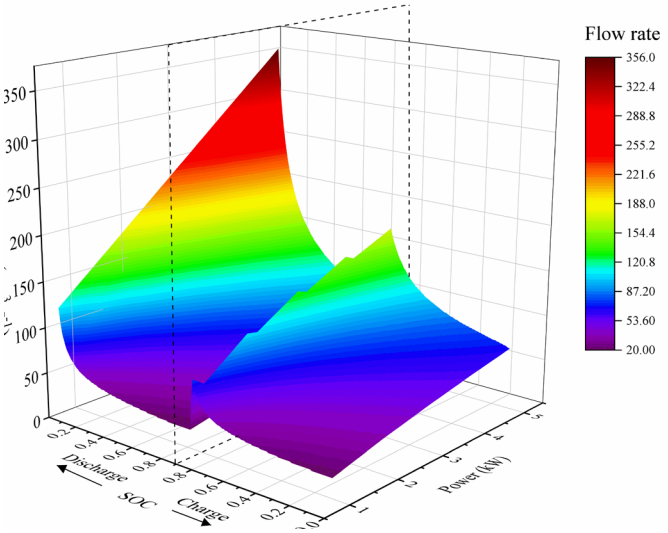

Fig. 8. Optimal flow rate surface under various charge/discharge power.

Since frequent tuning of pumps could increase the failure rate of the devices, an adjustment rule needs to be set up to ensure high reliability and high efficiency of the system. The analysis of power losses is first carried out to understand how the concentration overpotential varies under different SOCs. Simulations were conducted under a fully charged/discharged cycle with a constant power of 4 kW. Two constant flow rates (100 $cm^3 \cdot s^{-1}$ and 200 $cm^3 \cdot s^{-1}$) were applied. As shown from the results in Fig. 9, at high SOC levels where there are sufficient active vanadium ions in the solution, the concentration overpotential is not high compared to those caused by other types of power losses. However, when the SOC is below 0.7 during the charging process or when the SOC is above 0.3 during the discharging process, the active vanadium ions tend to deplete, leading to considerable power loss due to the significantly increased concentration overpotential. Thus, reducing the concentration overpotential by adjusting the flow rate may not always benefit the whole charging/discharging process. The flat bottom of flow rate in Fig. 8 also indicates that the pumps do not need to be adjusted in the high SOC region.

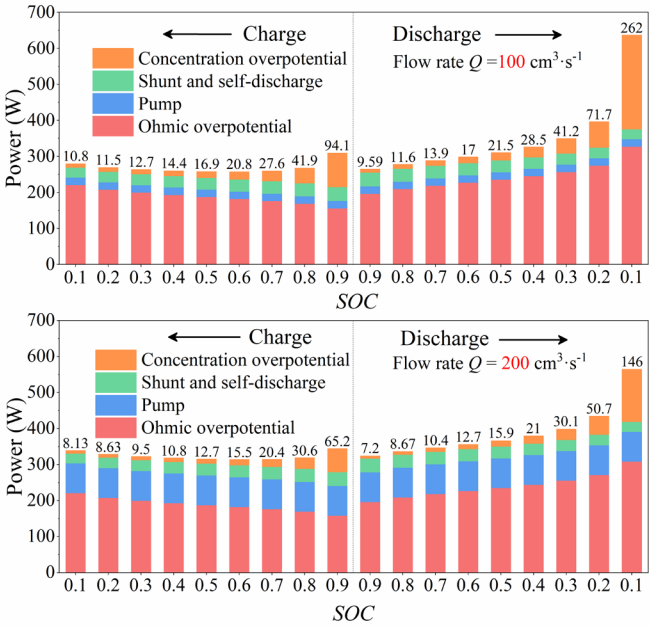

Fig. 9. Power losses in VRB charging and discharging process.

Therefore, we propose to maintain a constant flow rate when the SOC sits between 0.3 and 0.7, while only adjust the flow rate when the SOC is beyond this range.

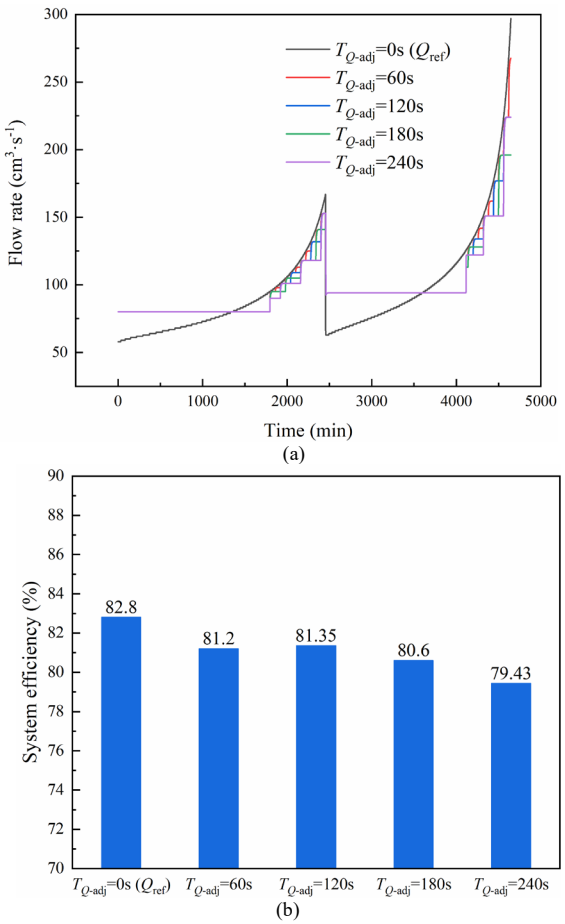

Fig. 10. Sensitivity analysis for adjustment period of flow rate. (a) Optimal flow rate under different adjustment periods. (b) Round-trip system efficiency under different adjustment periods.

TABLE VI
PARAMETERS OF PI CONTROLLERS

Coefficient	Value
$k_{i,I}$	0.1
$k_{i,Q}$	0.01
$k_{p,I}$	0.5
$k_{p,Q}$	0.2

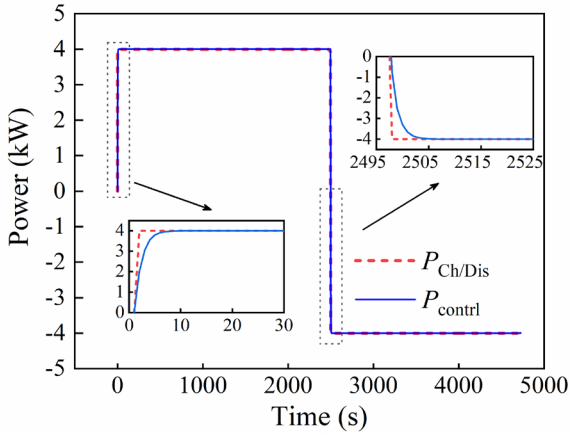

Fig. 11. Proposed two-stage control strategy under constant power of 4 kW with an adjustment period of 120 s.

The next step is to determine an appropriate adjustment period T_{Q_adj} for the pumps at Stage 2. The parameters of the closed-loop PI controller used in the simulation are listed in Table VI. A sensitivity analysis of T_{Q_adj} was carried out under a constant power of 4 kW with four different T_{Q_adj} of 60, 120, 180, and 240 s. The optimal flow rates and the round-trip system efficiencies with different T_{Q_adj} are shown in Fig. 10(a) and Fig. 10(b), respecively. It is observed in Fig. 10(b) that the system efficiency under T_{Q_adj} = 120 s is the highest of all cases. However, it is still lower than the global optimal, Q_{ref}, which is obtained from Stage 1. This is due to a trade-off between system efficiency and pump reliability. Thus, T_{Q_adj} = 120 s is adopted in this paper as the adjustment period.

The system dynamic behavior using the proposed two-stage control strategy is plotted in Fig. 11. The battery is charging/discharging under a constant flow rate before the SOC has reached a specific operating point, and then the flow rate is adjusted periodically under T_{Q_adj} = 120 s. The controlled power is tracking with the reference power of 4 kW and reaches a steady-state within 5 s, demonstrating that the control strategy has a good power tracking ability.

C. Case Study for Smoothing Wind Power Generation

In this section, the effectiveness of the proposed two-stage control strategy for VRB-ESSs is evaluated in a practical scenario. For grid applications, the VRB-ESSs are usually integrated with renewable energy generators, such as wind turbines and solar photovoltaics, to smooth out the power fluctuations and participate in grid regulation [33, 34].

The schematic of a 600-kW/1200-kWh VRB-ESS coupled with a 2-MW wind turbine generator for simulation is shown in Fig. 12. Note that the simulation is done based on Matlab Simulink 2020a to validate the effectiveness of the proposed control method. The wind power data for one day is first

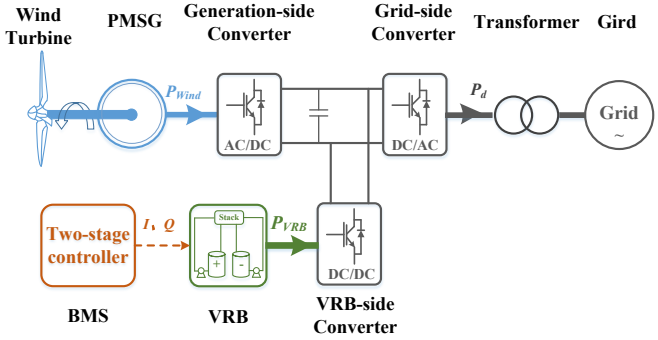

Fig. 12. Schematic of the wind-VRB system under simulation investigation.

extracted from [28]. Then, the fluctuating wind power is smoothened using low-pass filtering.

Next, the resulting high-frequency components are absorbed or supplied by the VRB system. The smoothened wind power is finally delivered to the power grid.

The fluctuating wind power is smoothened by using low-pass filtering, and the high-frequency components are delivered to the VRB system. The wind power, VRB power, and grid power profile are illustrated in Fig.13(a). In this scenario, the proposed two-stage control strategy is compared with four existing control strategies, including the traditional constant-flow-rate strategy and three flow-rate-factor strategies (flow factor, FF = 3,5,7). The assigned power to the VRB system and the *ISE*s based on different strategies are shown in Fig. 13(b), while Fig. 13(c) shows its detail between 16 h and 17 h. Compared to the other four strategies, the proposed two-stage control strategy can obtain the highest *ISE*. In contrast, the constant flow rate strategy demonstrates the worst performance since its *ISE* may drop to a very low value. The main reason is that the concentration overpotential can be very high at a certain period, especially when the input/output power shifts to a high level. By comparing the *ISE*s obtained by the flow-rate-factor strategies, it is found that the difference between FF = 5 and the two-stage control strategy is the smallest, with a maximum difference of 17.5% and the minimum difference of 0.02%. Fig. 13(d) shows the average *ISE* obtained by several strategies at different operation times. The average *ISE*s of the two-stage control strategy at various adjustment periods are compared. In this paper, $T_{Q\text{-adj}}$ = 120 s is used, and the highest average *ISE* of 93.54% is achieved, followed by the flow factor strategy of FF = 5 with an *ISE* of 91.43%, within one day of the operation of the wind-VRB combined system. This indicates that the two-stage control strategy can effectively reduce the system losses during the operation of the wind-VRB system.

Since the high electrolyte temperature may cause vanadium ion precipitation, the temperatures of the stack, pipe, and heat exchanger need to be monitored to ensure a safe operation of the VRB system. The prediction results under the two-stage control strategy are shown in Fig. 14. The measured ambient temperature data outside the laboratory were used in the simulation. It is found that the stack temperature is always the highest among all internal temperatures. The maximum stack temperature is about 24.5 °C, which guarantees the VRB is operating in a safe range.

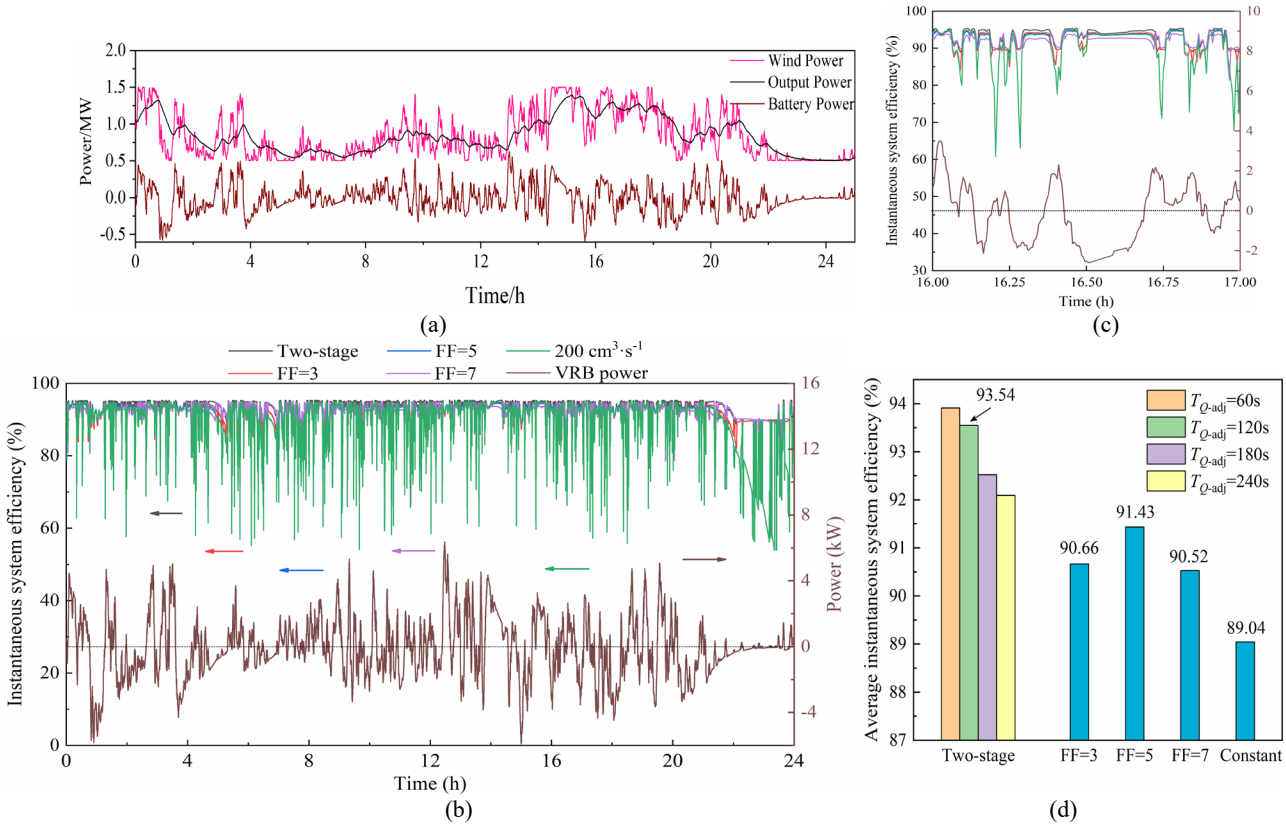

Fig. 13. Comparison of different control strategies under wind power fluctuation smoothing scenario. (a) Assigned wind power and VRB power during smoothing. (b) Assigned VRB power and instantaneous system efficiencies of five control strategies during a typical day. (c) Detail of the instantaneous system efficiency from 16 h to 17 h. (d) Average instantaneous system efficiency.

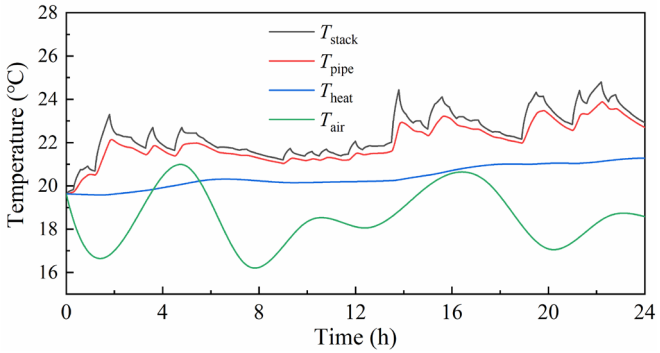

Fig. 14 Electrolyte temperature during a typical day under the two-stage control strategy.

V. Conclusion

Traditional VRB control strategies mainly focus on optimizing flow rates under constant current. Unfortunately, the operational conditions are much more complex in grid applications. The assigned power to the VRB system is constantly fluctuating, and tracking the optimal reference is always difficult due to the physical constraints of the pump systems. In this paper, a two-stage control strategy is designed for grid applications of VRB systems based on a multi-physics model under time-varying power demand. The two-stage control strategy consists of 1) a flow-rate control for regulating the pumped electrolyte transfer in a slow time scale and 2) a current control that regulates the chemical reactions in a fast time scale. The strategy shows high efficiency and high accuracy in tracking typical dynamic power profiles to smooth renewable generation, and there is an average of 2.1% increase of system instantaneous efficiency compared to the state-of-the-art strategies. These results demonstrate the effectiveness of the proposed control strategy and provide guidelines for novel VRB controller design. The proposed VRB control method can be implemented in the grid for various applications.

Appendix A

The key parameters of the electrical sub-model, including $E_0^{T_0}$, $R_{\text{ohm}}^{T_0}$, k_1, k_2, k_3, A_{ed}, and A_{ec}, are identified by minimizing the sum of square error between the stack voltage, $U_{\text{stack},k}$, simulated by using the proposed model and the measured stack voltage, $\hat{U}_{\text{stack},k}$, from the experiment, i.e.,

$$\min(J) = \min\left(\sum_k (U_{\text{stack},k} - \hat{U}_{\text{stack},k})^2\right) \tag{A.1}$$

subject to

$$\begin{cases} E_0^{T_0} \in [E_{0,\min}^{T_0}, E_{0,\max}^{T_0}] \\ R_{\text{ohm}} \in [R_{\text{ohm},\min}, R_{\text{ohm},\max}] \\ k_j \in [k_{j,\min}, k_{j,\max}], \quad j \in \{1,2,3\} \\ A_{\text{ed}} \in [A_{\text{ed},\min}, A_{\text{ed},\max}] \\ A_{\text{ec}} \in [A_{\text{ec},\min}, A_{\text{ec},\max}] \end{cases}$$

The particle swarm optimization (PSO) method is used to solve the above optimization problem [28]. The procedure is described below.

Step 1: Initialize a population of M particles. The initial population of the swarm group is randomly generated and follows the uniform distribution. The position of the ith particle is assigned as,

$$X_i = [E_{0,i}^{T_0} \quad R_{\mathrm{ohm},i} \quad k_{1,i} \quad k_{2,i} \quad k_{3,i} \quad A_{\mathrm{ec},i} \quad A_{\mathrm{ed},i}] \tag{A.2}$$

Step 2: Evaluate the fitness of each particle by (A.1);

Step 3: Determine the individual best position X_i^{pb} to obtain the minimum error,

$$X_i^{\mathrm{pb}} = \arg\left\{\min J(X_k^{\mathrm{pb}}), k = 0,1,2,\cdots,i\right\} \tag{A.3}$$

Similarly, the global best position X_i^{pb} is determined by

$$X_i^{\mathrm{pb}} = \arg\left\{\min J(X_k^{\mathrm{pb}}), k = 0,1,2,\cdots,i\right\} \tag{A.4}$$

Step 4: Calculate the velocities of the particles, v_i, and positions, X_i, by applying the following equations, respectively,

$$\begin{cases} v_{i+1} = \omega \cdot v_i + c_1 r_1 [X_i^{\mathrm{pb}} - X_i] + c_2 r_2 [X_i^{\mathrm{pb}} - X_i] \\ X_{i+1} = X_i + v_{i+1} \end{cases} \tag{A.5}$$

where ω denotes the inertia weight, c_1 and c_2 are learning factors, and r_1 and r_2 are random numbers within (0,1].

Step 5: Repeat Step 2 to Step 4 until the fitness J meets the convergence criterion. If the error reaches the convergence value, the global solution of the particle X_i^{pb} is obtained.

The initial PSO parameters are shown in Table A-1.

TABLE A-1. PARAMETERS OF PSO

PSO Parameter	Description	Value
M	Particle number	50
ω	Inertia weight	1
c_1	Learning factor	2
c_2	Learning factor	2

APPENDIX B

The key parameters of the thermal sub-model were obtained based on the method proposed in [28]. The heat is transferred from the stack to the tanks by electrolyte via the hydraulic pipes and heat exchanger. The schematized using an equivalent thermal circuit is shown in Fig. A-1.

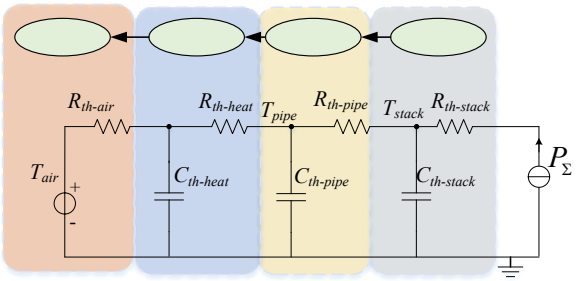

Fig. A-1. Schematic of a third-order Cauer network.

According to the principle of electrothermal analogy, heat flux is considered as current. The thermal sub-model is set up using a third-order Cauer network to mimic the overall heat transfer process from the stack to the ambient via the pipes and the heat exchangers. The obtained thermal resistances and thermal capacitances in the Cauer network are given in Table IV.

REFERENCES

[1] H. Zhao, Q. Wu, S. Hu, H. Xu, and C. N. Rasmussen, "Review of energy storage system for wind power integration support," *Appl. Energy*, vol. 137, pp. 545-553, 2015.

[2] X. Li, R. Ma, W. Gan and S. Yan, "Optimal dispatch for battery energy storage station in distribution network considering voltage distribution improvement and peak load shifting," *J. Modern Power Syst. Clean Energy*, vol. 10, no. 1, pp. 131-139, 2022.

[3] M. Li, Y. Li, and S. S. Choi, "Dispatch planning of a wide-area wind power-energy storage scheme based on ensemble empirical mode decomposition technique," *IEEE Trans. Sustain. Energy*, vol. 12, no. 2, pp. 1275-1288, 2021. doi: 10.1109/TSTE.2020.3042385.

[4] T. Horiba, "Lithium-ion battery systems," *Proc. IEEE*, vol. 102, no. 6, pp. 939-950, Jun. 2014.

[5] Basile, A., Iulianelli, A., Eds. Hydrogen Production by Water Electrolysis. "Advances in Hydrogen Production, Storage and Distribution"; Woodhead Publishing, 2014; pp 159–185.

[6] Z. Wei, J. Zhao, and B. Xiong, "Dynamic electro-thermal modeling of all-vanadium redox flow battery with forced cooling strategies," *Appl. Energy*, vol. 135, pp. 1-10, 2014.

[7] R. Ye, D. Henkensmeier, S. J. Yoon, Z. Huang, D. K. Kim, Z. Chang, S. Kim, and R. Chen, "Redox flow batteries for energy storage: A technology review," *J. Electrochem. Energy Convers. Storage*, vol. 15, no. 1, 2017

[8] B. Xiong, J. Zhao, Y. Su, Z. Wei, and M. Skyllas-Kazacos, "State of charge estimation of vanadium redox flow battery based on sliding mode observer and dynamic model including capacity fading factor," *IEEE Trans. Sustain. Energy*, vol. 8, no. 4, pp. 1658-1667, 2017.

[9] Z. Xu et al., "An advanced integrated electrode with micron- and nano-scale structures for vanadium redox flow battery," *J. Power Sources*, vol. 450, pp. 227686, 2020.

[10] Y. Shi et al., "Recent development of membrane for vanadium redox flow battery applications: A review," *Appl. Energy*, vol. 238, pp. 202-224 2019.

[11] H. Chen, S. Wang, H. Gao, X. Feng, C. Yan, and A. Tang, "Analysis and optimization of module layout for multi-stack vanadium flow battery module," *J. Power Sources*, vol. 427, pp. 154-164, 2019.

[12] Z. Wei, B. Xiong, D. Ji, and K. J. Tseng, "Online state of charge and capacity dual estimation with a multi-timescale estimator for lithium-ion battery," *Energy Procedia,* vol. 105, pp. 2953-2958, 2017.

[13] A. Lucas and S. Chondrogiannis, "Smart grid energy storage controller for frequency regulation and peak shaving, using a vanadium redox flow battery," *Int. J. Electr. Power Energy Syst.*, vol. 80, pp. 26-36, 2016.

[14] Y. Li, X. Zhang, J. Bao, and M. Skyllas-Kazacos, "Studies on optimal charging conditions for vanadium redox flow batteries," *J. Energ. Storage*, vol. 11, pp. 191-199, 2017.

[15] S. Han and L. Tan, "Thermal and efficiency improvements of all vanadium redox flow battery with novel main-side-tank system and slow pump shutdown," *J. Energ. Storage*, vol. 28, pp. 101274, 2020.

[16] C. Y. Ling, H. Cao, M. L. Chng, M. Han, and E. Birgersson, "Pulsating electrolyte flow in a full vanadium redox battery," *J. Power Sources*, vol. 294, pp. 305-311, 2015.

[17] X. Ma, H. Zhang, C. Sun, Y. Zou, and T. Zhang, "An optimal strategy of electrolyte flow rate for vanadium redox flow battery," *J. Power Sources*, vol. 203, pp. 153-158, 2012.

[18] A. Tang, J. Bao, and M. Skyllas-Kazacos, "Studies on pressure losses and flow rate optimization in vanadium redox flow battery," *J. Power Sources*, vol. 248, pp. 154-162, 2014.

[19] S. König, M. R. Suriyah, and T. Leibfried, "Innovative model-based flow rate optimization for vanadium redox flow batteries," *J. Power Sources*, vol. 333, pp. 134-144, 2016.

[20] W. Xiao and L. Tan, "Control strategy optimization of electrolyte flow rate for all vanadium redox flow battery with consideration of pump," *Renew. Energy*, vol. 133, pp. 1445-1454, 2019.

[21] Y. Li, X. Zhang, J. Bao, and M. Skyllas-Kazacos, "Control of electrolyte flow rate for the vanadium redox flow battery by gain scheduling," *J. Energy Storage*, vol. 14, pp. 125-133, 2017.

[22] M. Pugach, S. Parsegov, E. Gryazina, and A. Bischi, "Output feedback control of electrolyte flow rate for vanadium redox flow batteries," *J. Power Sources*, vol. 455, pp. 227916, 2020.

[23] R. Badrinarayanan, K. J. Tseng, B. H. Soong, and Z. Wei, "Modelling and control of vanadium redox flow battery for profile based charging applications," *Energy*, vol. 141, pp. 1479-1488, 2017.

[24] T. Wang, J. Fu, M. Zheng, and Z. Yu, "Dynamic control strategy for the electrolyte flow rate of vanadium redox flow batteries," *Appl. Energy*, 2017.
[25] T. Jirabovornwisut and A. Arpornwichanop, "A review on the electrolyte imbalance in vanadium redox flow batteries," *Int. J. Hydrogen Energy*, vol. 44, no. 45, pp. 24485-24509, 2019.
[26] Z. Wei, J. Zhao, M. Skyllas-Kazacos, and B. Xiong, "Dynamic thermal-hydraulic modeling and stack flow pattern analysis for all-vanadium redox flow battery," *J. Power Sources*, vol. 260, pp. 89-99, 2014.
[27] X. Qiu, T. A. Nguyen, J. D. Guggenberger, M. L. Crow, and A. C. Elmore, "A field validated model of a vanadium redox flow battery for microgrids," *IEEE Trans. Smart Grid*, vol. 5, no. 4, pp. 1592-1601, 2014.
[28] B. Xiong et al., "An enhanced equivalent circuit model of vanadium redox flow battery energy storage systems considering thermal effects," *IEEE Access*, vol. 7, pp. 162297-162308, 2019.
[29] X. Qiu, M. L. Crow, and A. C. Elmore, "A balance-of-plant vanadium redox battery system model," *IEEE Trans. Sustain. Energy*, vol. 6, no. 2, pp. 557-564, 2015.
[30] M. Pugach, M. Kondratenko, S. Briola, and A. Bischi, "Zero dimensional dynamic model of vanadium redox flow battery cell incorporating all modes of vanadium ions crossover," *Appl. Energy*, vol. 226, pp. 560-569, 2018.
[31] A. Trovò et al., "Standby thermal model of a vanadium redox flow battery stack with crossover and shunt-current effects," *Appl. Energy*, vol. 240, pp. 893-906, 2019-01-01, 2019.
[32] B. Xiong, J. Zhao, K. J. Tseng, M. Skyllas-Kazacos, T. M. Lim, and Y. Zhang, "Thermal hydraulic behavior and efficiency analysis of an all-vanadium redox flow battery," *J. Power Sources*, vol. 242, pp. 314-324, 2013.
[33] J. Liu, W. Yao, J. Wen, J. Fang, L. Jiang, H. He, S. Cheng, "Impact of power grid strength and PLL parameters on stability of grid-connected DFIG wind farm," *IEEE Trans. Sustain. Energy*, vol. 11, no. 1, pp. 545-557, 2020-01-01, 2020.
[34] B. Zhou, J. Fang, X. Ai, C. Yang, W. Yao, J., Wen, "Dynamic var reserve-constrained coordinated scheduling of LCC-HVDC receiving-end system considering contingencies and wind uncertainties," *IEEE Trans. Sustain. Energy*, vol. 12, no. 1, pp. 469-481, 2021.

Binyu Xiong (Member, IEEE) received the M.Sc. and Ph.D. degrees in power engineering from Nanyang Technological University, Singapore, in 2011 and 2016, respectively. He is currently an associate professor in the School of Automation, Wuhan University of Technology, Wuhan, China. His research interests include electrical and thermal modeling of batteries, battery system control, large-scale energy storage systems, and renewable energy generations.

Jinrui Tang (Member, IEEE) received the B.S. degree in electrical engineering from Zhejiang University, Hangzhou, China, in 2009, and the Ph.D. degree in electrical engineering from the School of Electrical and Electronics Engineering, Huazhong University of Science and Technology, Wuhan, in 2014. He is currently an Associate Professor with the School of Automation, Wuhan University of Technology, Wuhan. His research interests include power system protection, distribution system, and energy storage system.

Yang Li (Member, IEEE) received the B.E. degree in electrical engineering from Wuhan University, Wuhan, China, in 2007 and the Ph.D. degree in power engineering from Nanyang Technological University (NTU), Singapore, in 2015. From 2015 to 2018, he was a Research Fellow with the Energy Research Institute, NTU, and the School of Electrical Engineering and Computer Science, Queensland University of Technology, Brisbane, Australia, respectively. In 2019, he joined the School of Automation, Wuhan University of Technology, Wuhan, as a faculty member. He is currently a Researcher at the Chalmers University of Technology, Gothenburg, Sweden. His research interests include modeling and control of renewable generation systems, energy storage systems, and power electronic converters.

Changjun Xie received the Ph.D. degree in vehicle engineering from the Wuhan University of Technology (WHUT), Wuhan, Hubei, China. From 2012 to 2013, he was a Visiting Scholar with the UC Davis, CA, USA. He is currently a Professor with the School of Automation, WHUT. He is currently the Director of the Institute of New Energy Detection and Control Technology, WHUT. His research interests include the new energy technology and the optimization of energy management in new energy vehicles.

Zirui Wang received the Master's degree in electrical engineering in the School of Automation, Wuhan University of Technology, Wuhan, China, in 2021. He is currently working in Jiangmen Pengjiang Power Supply Bureau of Guangdong Power Grid Co., Ltd. His research interests include electrical and thermal modeling of batteries, battery operation optimization strategy.

Xinan Zhang (Member, IEEE) received the B.E. degree in electrical engineering and automation from Fudan University, China, in 2008, and the Ph.D. degree from Nanyang Technological University (NTU), Singapore, in 2014. Then, he worked as a Postdoctoral Researcher with NTU and the University of New South Wales from 2014 to 2017. He worked as a Lecturer with NTU from June 2017 to September 2019. Since September 2019, he joined the University of Western Australia as a Senior Lecturer. His research interests include electrical machine drives, control and modulation of power electronic converters, and management of hybrid energy storage systems.

Hoay Beng Gooi (Life Senior Member, IEEE) received the B.S. degree in electrical engineering from National Taiwan University in 1978, the M.S. degree from the University of New Brunswick in 1980, and the Ph.D. degree in power engineering from the Ohio State University in 1983. From 1983 to 1985, he was an Assistant Professor with the Department of Electrical Engineering, Lafayette College. In 1991, he joined the School of Electrical and Electronic Engineering, Nanyang Technological University, Singapore, as a Senior Lecturer, where he has been an Associate Professor since 1999 and the Deputy Head of Power Engineering Division from 2008 to 2014. Since 2020, he has been Co-Director of SP Group-NTU Joint Lab. His current research interests include microgrid energy management systems, electricity markets, spinning reserve, energy storage, and renewable energy.